RSC Advances

PAPER

View Article Online
View Journal | View Issue

Cite this: *RSC Adv.*, 2024, **14**, 19294

Electron transfer at the heterojunction interface of CoP/MoS_2 for efficient electrocatalytic hydrogen evolution reaction†

Lili Zhang,[a] Aijiao Xu,[a] Xinxing Shi,[a] Huanhuan Zhang,[a] Zongpeng Wang,[a] Shijie Shen,[a] Jitang Zhang *[abc] and Wenwu Zhong *[a]

Received 11th April 2024
Accepted 13th May 2024

DOI: 10.1039/d4ra02712d

rsc.li/rsc-advances

Modulating the electronic states of electrocatalysts is critical for achieving efficient hydrogen evolution reaction (HER). However, how to develop electrocatalysts with superior electronic states is an urgent challenge that must be addressed. Herein, we prepared the CoP/MoS_2 heterojunction with a microsphere morphology consisting of thin nanosheets using a facile two-step method. The catalyst's ultrathin nanosheet structure not only provides an extensive surface area for exposing active sites, but it also enables ion transport and bubble release. Electron transfer occurs between CoP and MoS_2, optimizing the heterojunction's charge distribution and enhancing the intermediates' adsorption capabilities. As a result, the CoP/MoS_2 heterojunction exhibits outstanding electrocatalytic hydrogen evolution activity with an overpotential of only 88 mV at a current density of 10 mA cm^{-2}, which exceeds both the sulfide heterojunction Co_9S_8/MoS_2 and the phosphide heterojunction CoP/$CoMoP_2$. The experimental results and DFT calculation results show that the former has stronger synergistic effects and higher HER activity. This work sheds light on the exploration of efficient heterojunction electrocatalysts with excellent electronic structures.

Introduction

Zero carbon emission is a crucial goal in the context of addressing environment pollution and climate warming.[1–3] Hydrogen energy produced by the electrocatalytic hydrogen evolution reaction (HER) is regarded as an excellent alternative fuel to traditional fossil fuel sources.[4–10] At present, Pt based materials are the most efficient catalysts for the HER. Nevertheless, the low quantity and high price of noble metals hinders their widespread use in HER. Developing highly-efficient and cost-effective catalysts is of great importance in shifting from fossil fuel-based energy to renewable hydrogen.[11–17] Electrocatalysts' electronic states can influence their ability to adsorb and activate water molecules, as well as the subsequent electron transfer process. As a result, studying and understanding the electronic states of electrocatalysts is critical for designing effective electrocatalysts for efficient hydrogen evolution reaction. The presence of a heterointerface between two materials with different electronic properties can create a gradient in the electron density. This gradient promotes charge transfer across the interface, influencing the redox behavior of the active sites and altering their valence states during HER.

Transition metal sulfides,[18–21] selenides,[22–24] phosphates,[25–27] carbides[28–30] and other compounds with high activity and conductivity have drawn a lot of attention in the field of hydrogen evolution catalysts. CoP is a promising catalyst for hydrogen evolution among transition metal compounds due to its high HER activity, excellent stability and excellent conductivity.[31,32] Nonetheless, some research indicates that slow reaction kinetics in HER process are caused by the significant binding energy of CoP and reaction intermediates, which may hinder the further improvement of its hydrogen evolution absorption capacity.[33–35] MoS_2 has been demonstrated to be a potential HER electrocatalyst among transition metal sulfides.[36–41] 2D MoS_2 exhibits unique electrical properties due to significant interaction between atoms, which allows the nanosheet to expose a large number of active sites. Unfortunately, MoS_2 is a semiconductor with the limited catalytic active site and low electrical conductivity prevent its widespread use in the electrolytic water industry. Heterostructures have unique catalytic properties of HER due to the advantages of synergistic effect and electronic structural control.[42,43] Therefore, the combination of CoP with MoS_2 to further boost catalytic performance by utilizing the synergistic effect of the two has been widely used. Guo *et al.*[44] developed a hollow CoP@MoS_2 heterogeneous nanoframework by combining MoS_2 on a CoP

[a]*Zhejiang Key Laboratory for Island Green Energy and New Materials, Taizhou University, Taizhou 318000, China. E-mail: zhangjt@tzc.edu.cn; zhongww@tzc.edu.cn*
[b]*ERA Co, Ltd., Taizhou 318020, China*
[c]*Zhejiang University, College of Chemical and Biological Engineering, Hangzhou 310027, China*

† Electronic supplementary information (ESI) available. See DOI: https://doi.org/10.1039/d4ra02712d

nanoframework obtained from a metal–organic framework nanostructure (ZIF-67). The overpotential of CoP@MoS_2 is 119 mV and the corresponding Tafel slope is only 49 mV dec^{-1} at 10 mA cm^{-2}. The remarkable catalytic activity is due to its unique structure, moderate composition ratio and strong contact between CoP and MoS_2, and also the large number of defects and disordered configurations. Although some reports on CoP/MoS_2 heterojunction hydrogen evolution catalysts have been published, the synthesis process is more complex.[45,46] Therefore, to preparation of simple and excellent CoP/MoS_2 catalyst for HER hydrogen evolution and the exploration of its related mechanism still need to be further carried out.

Herein, we fabricated phosphide and sulfide heterojunction CoP/MoS_2 with microsphere morphology. Meanwhile, the catalytic performance and mechanism of CoP/MoS_2 were described by experimentation and DFT calculation. The hydrogen evolution features of hybrid heterojunctions of phosphide CoP/$CoMoP_2$ and sulfide Co_9S_8/MoS_2 fabricated by the same precursor (CoMo-LDH) were compared with CoP/MoS_2. The results demonstrate that CoP/MoS_2 has better hydrogen evolution performance than CoP/$CoMoP_2$ and Co_9S_8/MoS_2.[47,48] At the current density of 10 mA cm^{-2}, the required overpotential of CoP/MoS_2 is only 88 mV. Various characterizations and DFT simulations reveal that heterojunctions consisting of phosphide and sulfide have stronger synergistic effects and better HER activities than phosphide heterojunctions and sulfide heterojunctions.

Results and discussions

The XRD pattern of CoP/MoS_2 hydrogen evolution catalyst prepared at 550 °C is shown in Fig. 1(a). By contrast to CoP

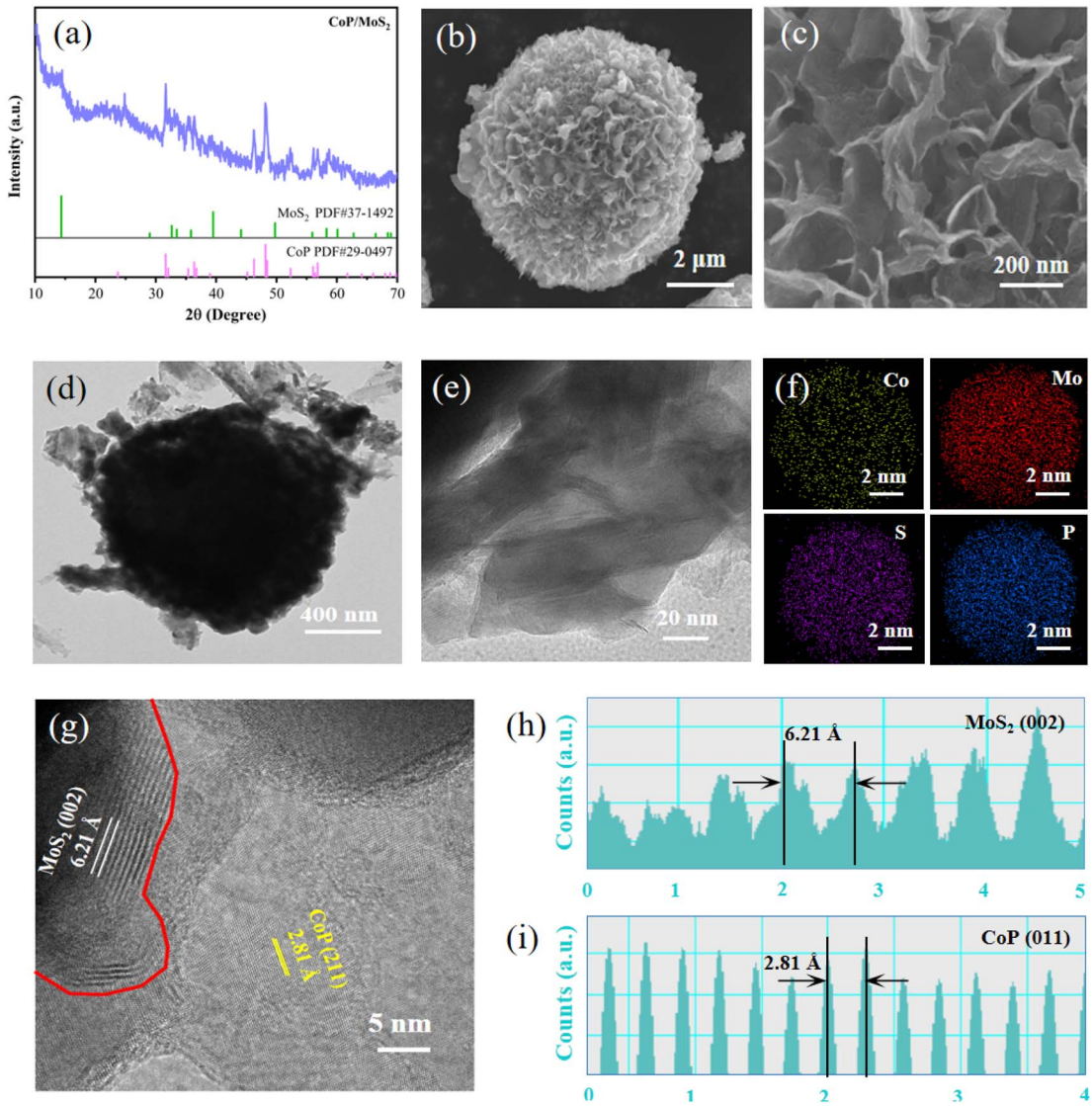

Fig. 1 (a) XRD patterns of CoP/MoS_2, (b and c) different magnifications of SEM images for CoP/MoS_2, (d and e) different magnifications of CoP/MoS_2 TEM images, (f) elemental mapping images of CoP/MoS_2, (g) HRTEM images for CoP/MoS_2, (h and i) CoP(011) and MoS_2(002) interplanar spacing.

standard data(PDF #29-0947), different samples exhibit discernible diffraction peaks at 2θ of 48.1° and 46.2°, matching the (211) and (112) crystal planes of CoP. Furthermore, all three samples exhibit comparable intensity diffraction peaks at the 2θ of 14.4°, which match to the (002) crystal face of MoS_2 (PDF #37-1492). Additionally, samples at 450 °C and 650 °C were prepared to investigate the effect of sulfuration and phosphorization temperatures on the products. As shown in Fig. S1(a),† samples prepared at 450 °C and 650 °C have no significant diffraction peaks, whereas the sample prepared at 550 °C have significant diffraction peaks and the best crystallinity, these results show that 550 °C is a suitable temperature to obtain the product. The EDS spectrum (Fig. S1(b)†) provides additional proof that the constituent components of the sample are Co, Mo, P and S. The presence of a small amount of O may be due to the insufficient vacuum degree in the quartz tube of the tube furnace, resulting in slight oxidation of the sample. SEM images of CoP/MoS_2 at different scales are displayed in Fig. 1(b and c). The sample has a microsphere-like shape and is covered in nanosheet structures. The cross-linked nanosheet structure can offer a better heterogeneous interface as well as the improved electronic conductivity. Fig. S2† displays SEM images of samples prepared at various temperatures and magnifications. It is clear that samples at 450, 550 and 650 °C retain the flower ball shape of the precursor. At 450 °C, the ultra-thin nanosheets on the surface of the flower ball are connected to each other and the sample nanosheets are more densely arranged. When the temperature reached 650 °C, the thickness of the nanosheets on the microspherical surface increased. Contraction and aggregation also took place at this temperature, which led to a reduction in the quantity of active sites and a decline in catalytic efficiency. The CoP/MoS_2 heterostructures prepared at 550 °C can be observed in TEM images with microspherical structures (Fig. 1(d)), and ultrathin nanosheet structures can be observed in enlarged images (Fig. 1(e)). The distribution of the Co, Mo, S and P elements in the sample is uniform, as seen in Fig. 1(f). High-resolution TEM images (Fig. 1(g)) reveal distinct fringes with the 6.21 Å fringe matching to the (002) crystal face of MoS_2 (Fig. 1(h)) and the 2.81 Å fringe corresponding to the (011) crystal face of CoP (Fig. 1(i)). There is a distinct interface between them, indicating the successful construction of a heterojunction.

Chemical compositions and elemental states of the samples were profiled using X-ray photoelectron spectroscopy (XPS). Fig. S3† displays the observed spectra of CoP, MoS_2 and CoP/MoS_2. Elemental components including Co, Mo, S, P and O are present in CoP/MoS_2 sample. The O element is formed by the oxidation of the sample surface, and the C element is formed by the toner added with the correction data. The Co^{2+} electrons are represented by the peaks near 781.9 eV and 798.1 eV in the high-resolution XPS spectrum of Co 2p (Fig. 2(a)), while the electrons of Co^{3+} are represented by the peaks at 777.8 eV and 793.8 eV.

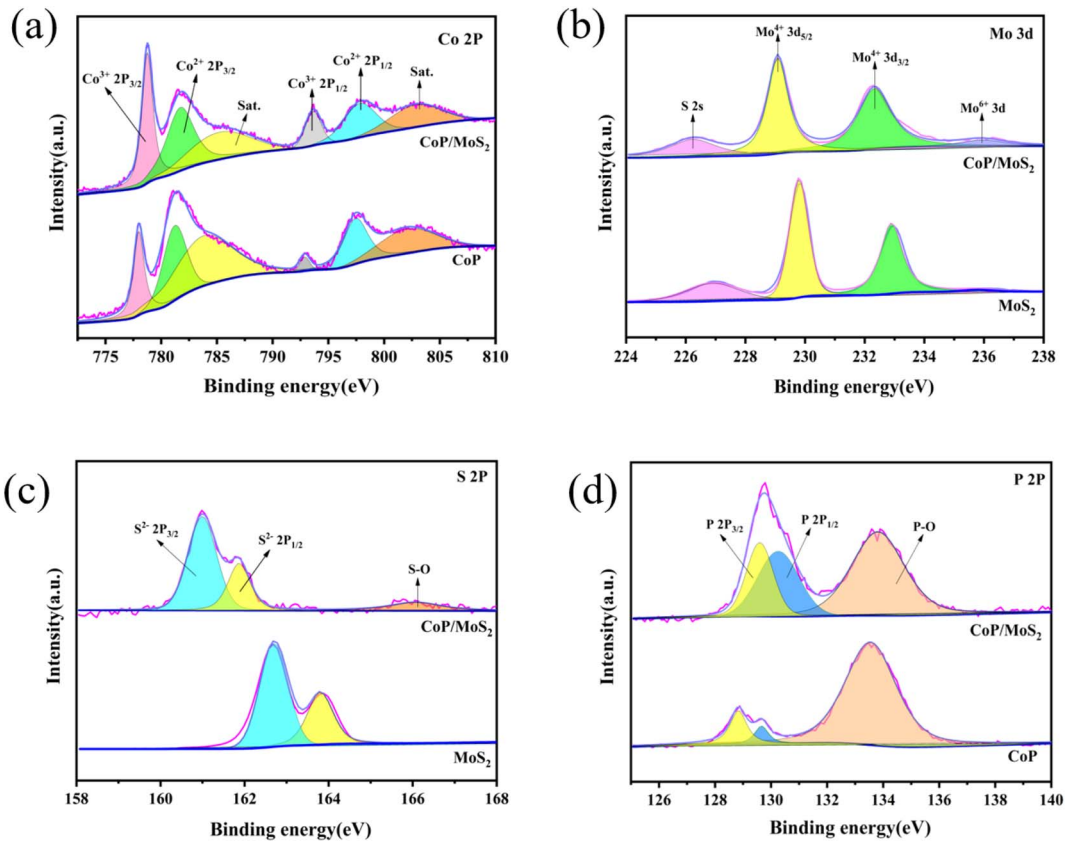

Fig. 2 (a) Co 2p high-resolution XPS spectra for CoP/MoS_2 and CoP, (b) Mo 3d high-resolution XPS spectra for CoP/MoS_2 and MoS_2, (c) P 2p high-resolution XPS spectra for CoP/MoS_2 and CoP, (d) S 2p high-resolution XPS spectra for CoP/MoS_2 and MoS_2.

Furthermore, the peaks from Co at 786.1 eV and 803.5 eV are satellite peaks. There is evidence that some electrons in CoP/MoS_2 are transported from Co to Mo, as the Co^{3+} peak area of CoP/MoS_2 is substantially greater than the Co^{3+} peak area of CoP. Four peaks are visible at 226.3 eV, 229.1 eV, 232.3 eV and 231.1 eV in the high-resolution XPS spectra of Mo (Fig. 2(b)). These peaks are assigned to S 2s, Mo^{4+} $3d_{5/2}$, Mo^{4+} $3d_{3/2}$ and Mo^{6+} 3d, respectively. In contrast to MoS_2, the Mo^{4+} 3d peak of CoP/MoS_2 moves in the direction of a lower binding energy, suggesting that Mo in CoP/MoS_2 receives electrons. The emergence of Mo^{6+} is caused by the oxidation of some Mo elements on the surface of the sample. P $2p_{3/2}$, P $2p_{1/2}$ and P–O are represented by the three peaks in the XPS spectra of high-resolution P 2p electrons (Fig. 2(c)), which are situated at 129.6 eV, 130.2 eV and 133.8 eV, respectively. CoP/MoS_2 exhibits an increase in P 2p peak area and a decrease in P–O peak area, a shift in peak location towards the direction of higher binding energy. The peaks between 160 and 165 eV in the XPS spectra of S 2p electrons (Fig. 2(d)) can be fitted with two peaks, which are S^{2-} $2p_{3/2}$ and S^{2-} $2p_{1/2}$ electrons, respectively. The S 2s peaks of CoP/MoS_2 migrate substantially in the direction of low binding energy as compared to MoS_2. The aforementioned findings demonstrate that the electrical structure of CoP/MoS_2 is optimized and that charge transfer occurs between CoP and MoS_2.

In general, the catalytic activity of HER of various materials is reflected by the corresponding overpotential at a current density of 10 mA cm^{-2}. As demonstrated by Fig. 3(a and b), samples at 450 °C, 550 °C and 650 °C have overpotentials of 104, 88 and 151 mV at a current density of 10 mA cm^{-2}, with corresponding Tafel slopes of 110.1, 87.5 and 162.3 mV dec^{-1}, respectively. According to the results of the LSV polarization curve and the Tafel slope results, the CoP/MoS_2 sample synthesized at 550 °C has the best catalytic performance. Meantime, the catalytic characteristics of phosphide/sulfide heterojunction CoP/MoS_2, phosphide heterojunction CoP/$CoMoP_2$, sulfide heterojunction Co_9S_8/MoS_2, as well as CoP and MoS_2 samples were compared. At 10 mA cm^{-2} current density, the LSV of each sample was 88, 94, 117, 137 and 254 mV, with the corresponding Tafel slopes of 85.7, 89.9, 92.6, 105.3 and 128.8 mV dec^{-1}. The results show that the catalytic performance of the CoP/MoS_2 hydrogen evolution catalyst is superior to the CoP/$CoMoP_2$ and Co_9S_8/MoS_2 hydrogen evolution catalysts, indicating that the CoP/MoS_2 sample has excellent HER kinetics. In order to determine the relatively effective electrochemically active surface area, the double-layer capacitance (C_{dl}) which is linearly proportional to the electrochemically active specific surface area (ECSA) is further measured. In previous research, C_{dl} of CoP/$CoMoP_2$, Co_9S_8/MoS_2, CoP and MoS_2 were evaluated and ECSA fitted at scanning rates of 0.02, 0.04, 0.08, 0.12, 0.16 and 0.20 V s^{-1}. Fig. 3(e) shows that their C_{dl} values are 30.3, 29.5, 16.5 and 7.47 mF cm^{-2}, respectively. CoP/MoS_2 samples was 40.9 mF cm^{-2}, showing that the CoP/MoS_2 heterojunction hydrogen evolution catalyst had a greater specific surface area of electrochemical activity, which considerably improved its hydrogen evolution performance. The electrochemical impedance of the prepared catalyst was measured in the range of 0.01 to 10^5 Hz. As shown in Fig. 3(f), the R_{ct} values of each sample are in the order from small to large: CoP/MoS_2(14.4 Ω), CoP/$CoMoP_2$(24.2 Ω), Co_9S_8/MoS_2(50.6 Ω), CoP(63.6 Ω) and MoS_2(189.8 Ω) indicate that the phosphide/sulfide heterojunction CoP/MoS_2 hydrogen evolution catalyst has lower charge transfer resistance than the sulfide and phosphide hydrogen evolution catalyst, which contributes to the rapid electron transfer in HER process. The stability of CoP/MoS_2 samples prepared at 550 °C in 1 M KOH solution was tested by constant point electrolysis method. As shown in Fig. 3(g), at the overpotential of 88 mV, the current density did not change significantly for more than 50 consecutive hours, indicating that the prepared CoP/MoS_2 heterojunction hydrogen evolution catalyst had excellent electrocatalytic hydrogen evolution stability, which was mainly due to the good binding force between CoP and MoS_2 substrate.

To further understand the mechanism of the enhancement of HER activity after CoP/MoS_2 forms heterogeneous structures, we use the Vienna Ab initio Simulation Package (VASP) for DFT calculation, Fig. S5† shows the optimized structure model of CoP, MoS_2 and CoP/MoS_2. Fig. S6(a)† shows the integral value of the density difference in *XY* cross sections of CoP/MoS_2 at different *Z* positions, which facilitates the quantification of the density difference distribution. It can be seen that the isosurface value of charge transfer at a fixed position is isosurface value = 0.005 e A^{-3}. Fig. S6(b)† depicts the CoP/MoS_2 differential charge density, where yellow and blue represent positive and negative charges, respectively. The yellow representing charge accumulation and blue representing charge consumption. It can be seen that electrons flow from CoP to MoS_2 and the charge distribution is optimized at the CoP/MoS_2 interface after forming a heterojunction. The improvement in heterojunction performance can be attributed to electronic structural optimization, which is consistent with the results of XPS results. Gibbs free energy (ΔG_{H^*}) is a appropriate parameter to evaluate HER activity of catalyst. To further investigate the HER activity of CoP/MoS_2 heterostructure hydrogen evolution catalysts, ΔG_{H^*} of CoP/MoS_2, CoP/$CoMoP_2$, Co_9S_8/MoS_2, CoP and MoS_2 were calculated (Fig. 4(a)). It can be seen that the ΔG_{H^*} of CoP/$CoMoP_2$, Co_9S_8/MoS_2, CoP and MoS_2 are 0.39 eV, −0.24 eV, 0.61 eV and 2.5 eV respectively, whereas CoP/MoS_2 is only 0.16 eV, which is very close to the ideal 0 eV, indicating that CoP/MoS_2 is the most favorable for HER reaction. The adsorption energy of the catalyst on water molecules is another parameter that reflects HER activity. As shown in Fig. 4(b), the adsorption energies of CoP/MoS_2, CoP/$CoMoP_2$, Co_9S_8/MoS_2, CoP and MoS_2 samples are −1.03 eV, −0.72 eV, −0.3 eV, −0.16 eV and 0.05 eV, respectively. The results indicate that Co_9S_8/MoS_2 exhibits the best adsorption of water molecules out of the three. This suggests that Co_9S_8/MoS_2 performs the best among these three in adsorbing water molecules. Both of hydrogen evolution free energy and water absorption energy of phosphating and sulfide heterojunction CoP/MoS_2 are superior to phosphating heterojunction CoP/$CoMoP_2$ and sulfide heterojunction Co_9S_8/MoS_2, indicating that phosphating/sulfide heterojunction CoP/MoS_2 have better synergistic effect and higher HER activity. Furthermore, we calculated Co, Mo, P and S atoms' partial density of states (PDOS) of CoP, MoS_2 and CoP/MoS_2. The systems all exhibit metal-like electronic characteristics (Fig. S7†). The

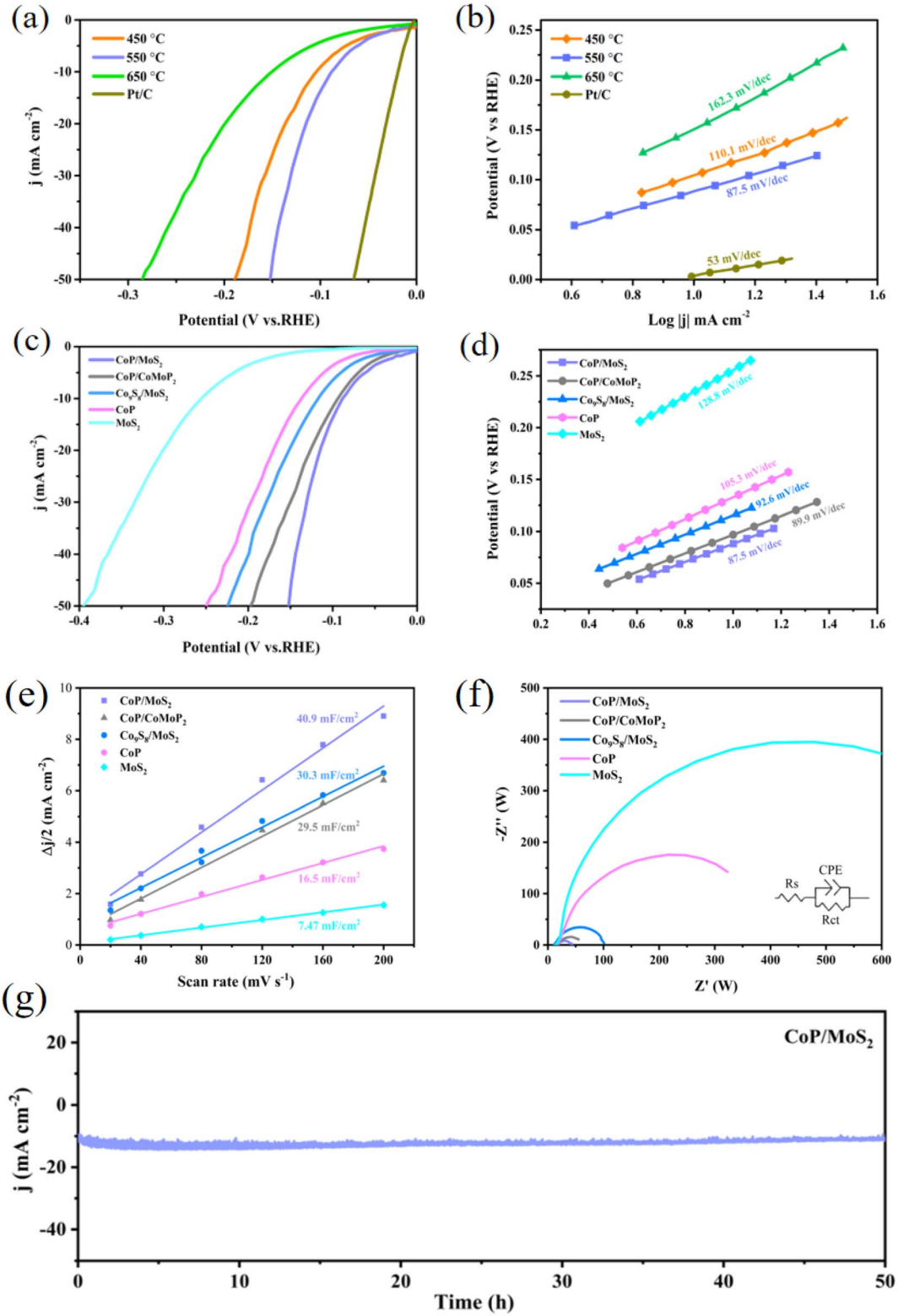

Fig. 3 (a and b) The polarization curves and related Tafel plots for CoP/MoS_2 at different temperatures, (c and d) the polarization curves and corresponding Tafel plots for CoP/MoS_2, $CoP/CoMoP_2$, Co_9S_8/MoS_2, CoP and MoS_2, (e) the double layer capacitance (C_{dl}) for CoP/MoS_2, $CoP/CoMoP_2$, Co_9S_8/MoS_2, CoP and MoS_2, (f) Nyquist plots for CoP/MoS_2, $CoP/CoMoP_2$, Co_9S_8/MoS_2, CoP and MoS_2, (g) the chronoamperometric curve for CoP/MoS_2 at 10 mA cm^{-2} current density in 1 M KOH.

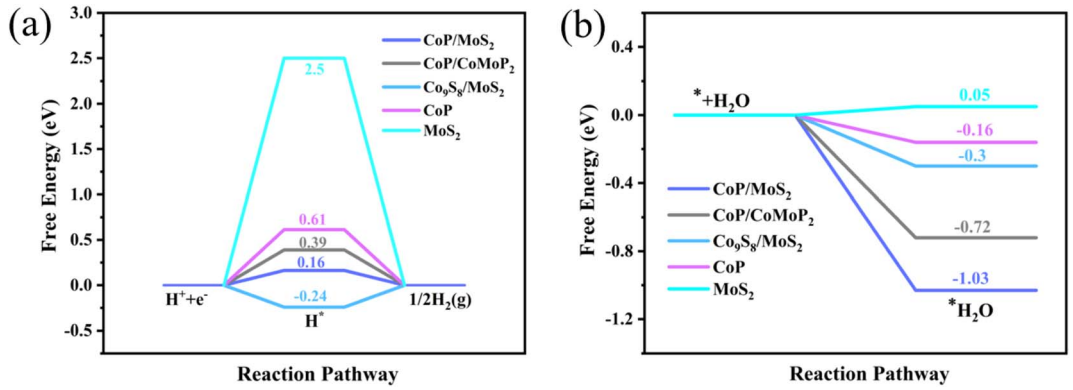

Fig. 4 (a) The ΔG_{H^*} and (b) for water adsorption energy for CoP/MoS_2, $CoP/CoMoP_2$, Co_9S_8/MoS_2, CoP and MoS_2.

density of states near the Fermi level of CoP/MoS_2 is lower than that of CoP and MoS_2. This suggests that it is not the conductivity of the heterojunction but the adsorption properties of its active sites that contribute to the superior performance.

Conclusion

In summary, we successfully synthesized CoP/MoS_2 microsphere heterojunction HER catalysts with a large number of nanosheets by phosphating and vulcanizing the CoMo-LDH precursor at different temperatures. The sample prepared at 550 °C shows the best crystallinity and surface morphology. The nanosheet structure on the microsphere's surface has an extensive surface area and fully exposed active sites. In addition, the charge transfer between CoP and MoS_2 optimizes the electronic state of the catalyst. As a result, the overpotential of CoP/MoS_2 is only 88 mV at a current density of 10 mA cm^{-2}, which is superior to that of the phosphides heterojunction $CoP/CoMoP_2$ and the sulfides heterojunction Co_9S_8/MoS_2. The findings suggest that CoP/MoS_2 has a stronger synergistic effect than the latter two. This work proposes a novel and simple way to fabricating high-performance transition metal-based compound heterojunctions.

Conflicts of interest

The authors declare no conflict of interest.

Acknowledgements

This work was financially supported by the National Natural Science Foundation of China (52072255, 22379104), Natural Science Foundation of Zhejiang Province, China (LY24E020004), China Postdoctoral Science Foundation (2022M723546), Taizhou University Excellent Youth Project (Z2020073).

References

1 O. Geden, *Nat. Geosci.*, 2016, **9**, 340–342.
2 J. Rogelj, M. Schaeffer, M. Meinshausen, R. Knutti, J. Alcamo, K. Riahi and W. Hare, *Environ. Res. Lett.*, 2015, **10**, 105007.
3 P. A. Koudakan, C. Wei, A. Mosallanezhad, B. Liu, Y. Y. Fang, X. B. Hao, Y. T. Qian and G. M. Wang, *Small*, 2022, **18**, 2107974.
4 F. Qureshi, M. Yusuf, A. A. Pasha, H. W. Khan, B. Imteyaz and K. Irshad, *Int. J. Hydrogen Energy*, 2022, **47**, 41397–41420.
5 R. K. Mishra, V. Kumar, L. G. Trung, G. J. Choi, J. W Ryu, P. Kumar, R. Bhardwaj, S. H. Lee and J. S. Gwag, *Mater. Lett.*, 2023, **338**, 134026.
6 F. Almomani, A. Al-Rababah, M. Tawalbeh and A. Al-Othman, *Fuel*, 2023, **332**, 125905.
7 P. K. Pathak, A. K. Yadav and S. Padmanaban, *Int. J. Hydrogen Energy*, 2023, **48**, 9921–9927.
8 M. Kim, Y. Kim, M. Y. Ha, E. Shin, S. J. Kwak, M. Park, I. D. Kim, W. B. Jun, W. B. Lee, Y. J. Kim and H. T. Jun, *Adv. Mater.*, 2023, 2211497.
9 J. M. Xiao, S. S. Zhang, Y. Y. Sun, X. T. Liu, G. L. He, H. Liu, J. Khan, Y. L. Zhu, Y. Q. Su, S. Y. Wang and L. Han, *Small*, 2023, **19**, 2206472.
10 H. B. He, L. B. Zeng, X. Y. Peng, Z. B. Liu, D. S. Wang, B. Yang, Z. J. Li, L. C. Lei, S. B. Wang and Y. Hou, *Chem. Eng. J.*, 2023, **451**, 138628.
11 L. L. Zhang, S. J. Shen, J. T. Zhang, Z. P. Lin, Z. P. Wang, Q. H. Zhang, W. W. Zhong, L. Zhu and G. F. Wu, *Small Methods*, 2022, 2200900.
12 L. L. Zhang, Z. P. Wang, J. T. Zhang, Z. P. Lin, Q. H. Zhang, W. W. Zhong and G. F. Wu, *Nano Res.*, 2023, **16**(5), 6552–6559.
13 Z. P. Lin, Z. P. Wang, J. J. Gong, T. C. Jin, S. J. Shen, Q. H. Zhang, J. C. Wang and W. W. Zhong, *Adv. Funct. Mater.*, 2023, **33**, 2307510.
14 S. J. Shen, Z. Y. Hu, H. H. Zhang, K. Song, Z. P. Wang, Z. P. Lin, Q. H. Zhang, L. Gu and W. W. Zhong, *Angew. Chem., Int. Ed.*, 2022, **61**, e202206460.
15 Z. X. Wu, P. F. Yang, Q. C. Li, W. P. Xiao, Z. J. Li, G. R. Xu, F. Liu, B. H. Jia, T. Y. Ma, S. H. Feng and L. Wang, *Angew. Chem., Int. Ed.*, 2023, **62**, e2023004.
16 K. Song, H. H. Zhang, Z. P. Lin, Z. P. Wang, L. L. Zhang, X. X. Shi, S. J. Shen, S. C. Chen and W. W. Zhong, *Adv. Funct. Mater.*, 2023, 2312672.

17 S. J. Shen, H. H. Zhang, K. Song, Z. P. Wang, T. T. Shang, A. Gao, Q. H. Zhang, L. Gu and W. W. Zhong, *Angew. Chem., Int. Ed.*, 2024, **63**, e20231534.
18 Y. M. Ding, N. W. Li, S. Yuan and L. Yu, *Chem.–Asian J.*, 2022, **17**, e202200178.
19 J. Xu, G. L. Shao, X. Tang, F. Lv, H. Y. Xiang, C. F. jing, S. Liu, S. Dai, Y. G. Li, J. Luo and Z. Zhou, *Nat. Commun.*, 2022, **13**, 2193.
20 M. Dar, K. Majid and M. Wahid, *New J. Chem.*, 2022, **46**, 22427–22440.
21 B. F. Chen, Y. C. Wang, S. J. Shen, W. W. Zhong, H. S. Lu and Y. Pan, *Small Methods*, 2024, 2301598.
22 X. Xiao, S. J. Shen, L. L. Zhang, Z. P. Lin, Z. P. Wang, Q. H. Zhang, W. W. Zhong and B. S. Zhan, *Chem.–Asian J.*, 2023, **18**, e202201182.
23 X. W. Pan, W. J. He, D. Cao, Y. Li, C. C. Liu, L. M. Liang, Q. Y. Hao and H. Liu, *ACS Appl. Nano Mater.*, 2023, **6**, 1724–1731.
24 A. Majumdar, P. Dutta, A. Sikdar, H. Lee, D. Ghosh, S. N. Jha, S. Tripathi, Y. Oh and U. N. Maiti, *Small*, 2022, **18**, 2200622.
25 T. W. Zhao, S. H. Wang, Y. B. Li, C. Jia, Z. Su, D. Hao, B. J. Ni, Q. Zhang and C. Zhao, *Small*, 2022, **18**, 2204758.
26 D. I. Jeong, H. W. Choi, J. Kim, U. Y. Lee, B. K. Koo, B. K. Kang and D. H. Yoon, *Appl. Surf. Sci.*, 2023, **614**, 156189.
27 Z. D. Li, C. Y. Zhang, Y. Yang, S. S. Pi, Y. J. Yu, C. F. Wan, B. Q. Zhou, W. X. Chao and L. Lu, *Inorg. Chem. Front.*, 2023, **10**, 325.
28 Y. F. Ma, M. Chen, H. B. Geng, H. F. Dong, P. Wu, X. M. Li, G. Q. Guan and T. J. Wang, *Adv. Funct. Mater.*, 2020, **30**, 2000561.
29 D. S. Baek, J. Y. Lee, J. J. Kim and S. H. Joo, *ACS Catal.*, 2022, **12**, 7415–7426.
30 S. Upadhya and O. P. Pandey, *J. Electrochem. Soc.*, 2022, **169**, 016511.
31 S. J. Shen, Z. P. Wang, Z. P. Lin, K. Song, Q. H. Zhang, F. Q. Meng, L. Gu and W. W. Zhong, *Adv. Mater.*, 2022, **34**, 2110631.
32 J. Q. Guo, C. Ouyang, Z. X. Zhan, T. Lei and P. Yin, *Int. J. Hydrogen Energy*, 2022, **47**, 181–196.
33 X. Z. Song, W. Y. Zhu, J. C. Ni, Y. H. Zhao, T. Zhang, Z. Q. Tan, L. Z. Liu and X. F. Wang, *ACS Appl. Mater. Interfaces*, 2022, **14**, 33151–33160.
34 L. H. Zhi, J. B. Tu, J. X. Li, M. Li and J. C. Liu, *J. Colloid Interface Sci.*, 2022, **616**, 379–388.
35 M. D. Wang, X. Y. Liu and X. Wu, *Nano Energy*, 2023, **114**, 108681.
36 X. Liu, Z. Q. Li, H. L. Jiang, X. Wang, P. F. Xia, Z. J. Duan, Y. Z. Ren, H. Y. Xiang, H. M. Li, J. Zeng, Y. G. Zhou and S. Liu, *Small*, 2023, 2307293.
37 H. J. Liu, S. Zhang, Y. M. Chai and B. Dong, *Angew. Chem., Int. Ed.*, 2023, **62**, e202313845.
38 K. J. Wang, Y. Jing, S. Gao, X. R. Liu, B. X. Liu, Y. C. Li, P. Zhang and B. H. Xu, *J. Colloid Interface Sci.*, 2023, **648**, 709–718.
39 J. Y. Shen, J. L. Zhang, G. N. Zhang, W. H. Li, M. Zheng, F. Y. Guo and Q. Q. Chen, *New J. Chem.*, 2022, **46**, 16419–16425.
40 K. Cao, S. W. Sun, A. Y. Song, J. X. Ba, H. W. Lin, X. H. Yu, C. Q. Xu, B. J. Jin, J. Huang and D. H. Fan, *J. Alloys Compd.*, 2022, **907**, 164539.
41 Y. Xu, J. Cheng, H. K. Lv, L. W. Ding, K. Zhang, A. N. Hu and X. Yang, *Chem. Eng. J.*, 2023, **470**, 144344.
42 G. Q. Zhao, K. Rui, S. X. Dou and W. P. Sun, *Adv. Funct. Mater.*, 2018, **28**, 1803291.
43 H. X. Wang, W. W. Fu, X. H. Yang, Z. Y. Huang, J. Li, H. J Zhang and Y. Wang, *J. Mater. Chem. A*, 2020, **8**, 6926.
44 T. Y. Xia, L. Zhou, S. Q. Gu, H. Gao, X. Y. Ren, S. F. Li, R. M. Wang and H. Z. Guo, *Mater. Des.*, 2021, **211**, 110165.
45 C. L. Zhang, Y. Xie, J. T. Liu, F. H. Cao, H. P. Cong and H. Li, *Chem. Eng. J.*, 2021, **419**, 129977.
46 J. G. Li, K. F. Xie, H. C. Sun, Z. S. Li, X. Ao, Z. H. Chen, K. K. Ostrikov, C. D. Wang and W. J. Zhang, *ACS Appl. Mater. Interfaces*, 2019, **11**, 36649–36657.
47 L. L. Zhang, X. X. Shi, A. J. Xu, W. W. Zhong, J. T. Zhang and S. J. Shen, *Nano Res.*, 2024, **17**(3), 2061–2069.
48 L. L. Zhang, J. T. Zhang, A. J. Xu, Z. P. Lin, Z. P. Wang, W. W. Zhong, S. J. Shen and G. F. Wu, *Biomimetics*, 2023, **8**, 104.